CCFE-PR(15)61

I. Toda-Caraballo, J.S. Wróbel, S.L. Dudarev, D. Nguyen-Manh, and
P.E.J. Rivera-Díaz-del-Castillo

Interatomic spacing distribution in multicomponent alloys

Interatomic spacing distribution in multicomponent alloys

I. Toda-Caraballo[1], J. S. Wróbel[2], S.L.Dudarev[2], D. Nguyen-Manh[2]
& P. E. J. Rivera-Diaz-del-Castillo[1]

[1] Department of Materials Science and Metallurgy, University of Cambridge, 27 Charles Babbage Rd, Cambridge, CB3 OFS, UK

[2] CCFE, Culham Science Centre, Abingdon, Oxon, OX14 3DB, UK

Interatomic spacing distribution in multicomponent alloys

I. Toda-Caraballo[1], J. S. Wróbel[2], S.L. Dudarev[2],

D. Nguyen-Manh[2] & P. E. J. Rivera-Díaz-del-Castillo[*,1]

[1] Department of Materials Science and Metallurgy, University of Cambridge

27 Charles Babbage Rd, Cambridge, CB3 0FS, UK

[2] CCFE, Culham Science Centre

Abingdon, Oxon OX14 3DB, UK

[*] P. E. J. Rivera-Díaz-del-Castillo[*,1] E-mail: pejr2@cam.ac.uk. Tel: +44 1223 331538

Abstract

A methodology to compute the distribution of interatomic distances in highly concentrated multicomponent alloys is proposed. By using the unit cell parameter and bulk modulus of the elements involved, the method accurately describes the distortion in the lattice produced by the interaction of the different atomic species. To prove this, density functional theory calculations have been used to provide the description of the lattice in a monophasic BCC MoNbTaVW high entropy alloy and its five sub-quaternary systems at different temperatures. Short-range order is also well described by the methodology, where the mean error in atomic coordinates with respect to the atomistic simulations is in the order of 1–2 pm over all compositions and temperatures considered. The new method can be applied to tailor solid solution hardening, highly dependent on the distribution of interatomic distances, and guide the design of new high entropy alloys with enhanced properties.

Keywords: High Entropy Alloys; Interatomic spacing; Density functional theory; Solid solution

hardening

1 Introduction

High Entropy Alloys (HEAs) are multicomponent systems incorporating several elements in a nearly equiatomic configuration. The content of each solute can typically vary between 5 and 35 at%. [1]. The high entropy associated with mixing several elements can inhibit the formation of intermetallic phases in favour of FCC or BCC solid solutions [2]. They show high strength and excellent wear resistance at low and high temperatures, which make them of great interest for many industrial applications [3, 4, 5, 6, 7, 8]. Yield strength and hardness in HEAs can display values in excess of 2000 MPa [9, 10] and 800 Hv [11], respectively. This high strength, usually at the expense of ductility, can be preserved even at high temperatures [5, 12, 13].

One of the main contributions to the yield strength in HEAs is solid solution hardening (SSH), which can be responsible for more than 50% of its value [14]. The SSH effect is explained for binary systems by Labush's approach [15] and has been extended to multicomponent alloys in a recent contribution [16]. This strengthening effect stems from the differences in atomic sizes and shear moduli of the elemental contributions, as described initially by Fleischer [17]. This affects the critical shear stress for dislocation glide and modifies the mechanical response of the material. Variations in the unit cell parameter and shear modulus in the neighbourhood of dislocation cores are the main interactions that impede dislocation movement. Among these variations, unit cell parameter alterations along the distorted lattice are the dominant factor in the proposed solid solution model [18].

An equation that predicts SSH in multicomponent alloys, denoted as $\Delta\sigma_{ss}$, was derived in [19]:

$$\Delta\sigma_{ss} = \left(\sum_i B_i^{3/2} X_i \right)^{2/3} \tag{1}$$

where X_i is the content of solute i and B_i is its hardening parameter, which is mainly dependent on the lattice distortion [18]. This methodology was used in [16] to successfully describe the SSH effect in more than 50 HEAs. In that work the matrix $S = \{s_{ij}\}$, as proposed by Moreen [20], was adopted, which describes the mean value of the distribution of nearest neighbour distances,

also called interatomic spacing distances, between atoms of different species in the alloy. Each individual interaction distance between atoms of type i and j can fluctuate over a range of values, depending on the combination of atoms and its coordinates around i and j. The averaged value of all i–j distances is captured by s_{ij} in matrix S. The matrix S is related to the mean interatomic spacing of the alloy s_{lat} by the frequency of occurrence of each i–j interaction. The contribution to the mean interatomic distance across the lattice by i–j interactions is therefore $s_{ij}X_iX_j$, where X_i and X_i are the content of elements i and j respectively, and X_iX_j the probability of occurrence of unions i–j in a solid solution:

$$s_{lat} = \sum_{i}^{n}\sum_{j}^{n} s_{ij}X_iX_j = (X_1, ..., X_n)\begin{pmatrix} s_{11} & s_{12} & \cdots & s_{1n} \\ s_{21} & s_{22} & \cdots & s_{2n} \\ \vdots & & \ddots & \vdots \\ s_{n1} & s_{n2} & \cdots & s_{nn} \end{pmatrix}\begin{pmatrix} X_1 \\ \vdots \\ X_n \end{pmatrix} \quad , \tag{2}$$

here, s_{lat} and the unit cell parameter a_{lat} are related by the atomic packing factor f:

$$s_{lat} = a_{lat}\ f \tag{3}$$

$f = \sqrt{3}/2$ for BCC and $f = 1/\sqrt{2}$ for FCC.

The description of the average distortion induced in the lattice by a solute or solutes is captured by the matrix S, the calculation of which is fundamental to the prediction of SSH and yield strength in multicomponent alloys. Plastic deformation depends also on the lattice configuration defined by this matrix S; other properties such as thermal expansion coefficient or electrical resistivity can be related to or influenced by this distortion.

The measurement of these lattice variations, which are required to determine matrix S with enough precision, is challenging from an experimental point of view. In an early work [20], Moreen showed that variations in interatomic spacing in a solid solution can be in the range of 2 pm, although most of the variations lie around 5-10 pm. A suitable technique for reaching this level of accuracy is high-energy X-ray diffraction produced by synchrotron radiation sources [21]. Nevertheless, it does not provide information on the relative atomic positions for the interactions. A

technique providing relative atomic positions is atom probe tomography, but it exhibits errors in the range of 2-3 Å. On the other hand, *ab initio* density functional theory (DFT) simulations have been used as a tool of extraordinary precision for describing many-body atomic systems [22, 23, 24] when structure relaxation is achieved. This technique can be combined with the cluster expansion (CE) method [23, 25] in order to reduce the lengthy simulation times of DFT.

The results have been used to describe and quantify with high accuracy lattice distortions in multicomponent alloys. Nevertheless, these techniques are very time consuming to be able to investigate hundreds or thousands of different compositions; a requirement for designing new HEAs. For this purpose, a methodology is presented in this work aiming at the prediction of interatomic distances in multicomponent alloys. The model presented here uses elemental unit cell parameters and bulk moduli to predict the average, over all atomic configurations in the lattice, of the nearest neighbour distance between different elements in a BCC lattice. This is done by using simplified expressions of the interatomic potentials, which assumes small displacements around equilibrium positions in a single crystal without defects. Six compositions have been considered, the equiatomic HEA MoNbTaVW and its 5 sub-quaternary systems at different temperatures. The elements involved are not too dissimilar and display solid solution BCC alloys on all compositions, as experimentally observed [26]. The atomic coordinates in the lattice are expected to be close to equilibrium. From this averaged lattice, a quasi-relaxed structure is then calculated displacing the atoms from mean positions to their individual equilibrium positions in the lattice by means of the local environment. This calculation is carried out by computing the vectorial form of the simplified expressions for the inteartomic potentials. The method shows a mean deviation around 1-2 pm in atomic positions with respect to DFT calculations. The high accuracy of this method provides an excellent description of the lattice, accompanied by a remarkable simplicity. This can support the DFT optimisation process providing a good starting point for the full relaxation of the lattice.

The paper is organised as follows. Section 2 explains the simulation method which combines *ab initio* DFT and CE methods. Section 3 shows an approximation to the *ab initio* BCC interatomic potentials by means of the elemental unit cell parameters and their bulk moduli. This is fundamental to the development of the methodology for the quasi-relaxed structure computation,

which is presented in section 4. First, we estimate the unit cell parameter for a given composition, and the mean interatomic distances between atoms of different species assuming a randomised atomic configuration; then, a numerical solver is applied to the equations derived from the vectorial form of the potentials to predict atomic positions at different temperatures, where short-range order (SRO) is predicted by atomistic simulations. Section 5 summarises the main conclusions and achievements.

2 First principles modelling of BCC HEAs

The analysis of the stability of single phase HEAs is a subject of great scientific interest for both experimental and modelling communities. However, just a few examples of single phase HEAs (FCC Fe-Cr-Mn-Ni-Co [27] or BCC W-Nb-Mo-Ta-V [26]), have been found. In most cases, the microstructure of the investigated alloys is not homogeneous [28] showing a non-uniform distribution of atoms. This is due to preferential interactions between atoms of different types. The uniformity of the BCC solution and the chemical ordering are investigated in the MoNbTaVW and sub-quaternary systems by means of the Cluster Expansion (CE) formalism in which the interaction between different elements can be determined from *ab-initio* calculations. At the obtained equilibrium configurations, the interatomic spacing distribution will be analysed.

2.1 Cluster Expansion method for multicomponent alloys

The phase stability of alloys is treated and analysed using a combination of density functional theory (DFT) calculations and lattice statistical mechanics simulations based on the Cluster Expansion (CE) method. In the CE formalism [23, 25, 29], the enthalpy of mixing ΔH_{mix} of a multicomponent alloy is evaluated using DFT, is defined as [29]

$$\Delta H_{mix}(\vec{\sigma}) = \sum_{\omega} m_{\omega} J_{\omega} \left\langle \Gamma_{\omega'}(\vec{\sigma}) \right\rangle_{\omega} , \tag{4}$$

where an atomic configuration is specified by a vector of the configurational variables $\vec{\sigma}$, the summation is performed over all the clusters ω distinct under group symmetry operations of the

underlying lattice, m_ω are multiplicities indicating the number of clusters equivalent to ω by symmetry (divided by the number of lattice sites), J_ω are the concentration-independent effective cluster interaction (ECI) parameters and $\langle \Gamma_{\omega'}(\vec{\sigma}) \rangle$ are the cluster functions defined as products of point functions of occupation variables on a specific cluster ω averaged over all the clusters ω' that are equivalent by symmetry to cluster ω.

The occupation variables and point functions [23, 29] are defined to allow the use of the same formulae for systems with different number of components. For an M-component system, the clusters $\gamma_{g,M}$ are

$$\gamma_{g,M}\left(\sigma_h\right) = \begin{cases} 1 & \text{if } g = 0 \ , \\ -\cos\left(2\pi \lceil \frac{g}{2} \rceil \frac{\sigma_h}{M}\right) & \text{if } g > 0 \text{ and odd}, \\ -\sin\left(2\pi \lceil \frac{g}{2} \rceil \frac{\sigma_h}{M}\right) & \text{if } g > 0 \text{ and even}, \end{cases} \tag{5}$$

where $\sigma_h = 0, 1, 2, \ldots, (M-1)$ are the elements of $\vec{\sigma}$, g is the index of point functions ($g = 0, 1, 2, \ldots, (M-1)$), and $\lceil \frac{g}{2} \rceil$ denotes denotes the ceiling function which maps a real number to its smallest following integer.

The cluster $\omega \equiv (|\omega|, n)$ is defined by the number of lattice points $|\omega|$, and the relative position of points denoted n. Each cluster ω can be decorated by different possible sequences of non-zero point functions, $(\zeta_{|\omega|,n}) = (g_1 g_2 ... g_{|\omega|})$. The number of possible decorations of a cluster is a permutation with repetitions $(M-1)^{|\omega|}$, although the number of non-equivalent decorations of the clusters is smaller due to the cluster symmetry. For example, interactions of pair clusters ($\gamma_{h,M}$,$\gamma_{g,M}$) and ($\gamma_{g,M}$,$\gamma_{h,M}$) are equivalent displaying $\frac{M!}{2!(M-2)!}$ occurrences without repetitions. In this work, we have used one point cluster, three pair clusters and one three-body cluster as shown in Figure 1a, providing 4, 10 and 40 possible decorations of point, pair and three-body clusters for five-component system. The enthalpy of mixing of a K-component system with the interactions of the considered clusters can be written as

$$\begin{aligned} \Delta H_{mix}(\vec{\sigma}) &= J_{1,1}^{(0)} + \sum_{(\zeta_{1,1})} m_{1,1}^{(\zeta_{1,1})} J_{1,1}^{(\zeta_{1,1})} \left\langle \Gamma_{1,1}^{(\zeta_{1,1})} \right\rangle + \sum_{(\zeta_{2,1})} m_{2,1}^{(\zeta_{2,1})} J_{2,1}^{(\zeta_{2,1})} \left\langle \Gamma_{2,1}^{(\zeta_{2,1})} \right\rangle + \sum_{(\zeta_{2,2})} m_{2,2}^{(\zeta_{2,2})} J_{2,2}^{(\zeta_{2,2})} \left\langle \Gamma_{2,2}^{(\zeta_{2,2})} \right\rangle \\ &+ \sum_{(\zeta_{2,3})} m_{2,3}^{(\zeta_{2,3})} J_{2,3}^{(\zeta_{2,3})} \left\langle \Gamma_{2,3}^{(\zeta_{2,3})} \right\rangle + \sum_{(\zeta_{3,1})} m_{3,1}^{(\zeta_{3,1})} J_{3,1}^{(\zeta_{3,1})} \left\langle \Gamma_{3,1}^{(\zeta_{3,1})} \right\rangle , \end{aligned} \tag{6}$$

where the sequence $(\zeta_{|\omega|,n}) = (g_1 g_2 ... g_{|\omega|})$ is the decoration of cluster $(|\omega|, n)$ by point functions, $\left\langle \Gamma_{|\omega|,n}^{(\zeta_{|\omega|,n})} \right\rangle$ and $J_{|\omega|,n}^{(\zeta_{|\omega|,n})}$ are the cluster function and the effective cluster interaction for a considered cluster decoration, and $J_{1,1}^{(0)}$ is the ECI parameter of zero point cluster.

The ECI $J_{|\omega|,n}^{(\zeta_{|\omega|,n})}$ parameters in five-component MoNbTaVW system were obtained by mapping DFT energies onto CE. A DFT database was generated from 428 structures for different BCC-like binaries, ternaries and quaternaries. The fitting procedure was performed using ATAT package [30] and the cross-validation error between DFT and CE was 8.4 meV/atom. Values of 30 two-body and 40 three-body ECI parameters for Mo-Nb-Ta-V-W alloys are given in Figure 1b. It is shown that the first and second nearest neighbour pair interactions are the most significant whereas the values of ECIs of the pair cluster with third nearest neighbours and the three-body cluster are much smaller. This indicates there is no need for further increasing the number of clusters.

This result differs with the analysis at [31, 32], where the order-disorder transition temperature was studied in the MoNbTaW system, and ternary and quaternary structures in the DFT database were ignored. This implies that only first neighbour interaction pairs were considered, neglecting the large significance of the second neighbour interaction.

DFT calculations were performed using the projector augmented wave (PAW) method implemented in VASP [33, 34]. Exchange and correlation were treated in the generalized gradient approximation GGA-PBE [35]. We used PAW potentials with semi-core p electron contribution with 11 electrons treated as valence for Ta, Nb and V and 12 electrons for W and Mo, which provide an excellent description of the elemental physical properties. The unit cell parameters and bulk moduli of the considered elements have been calculated. The bulk modulus is obtained from energy-volume per atom relations that are fitted with third-order Birch-Murnaghan equation of states [36],

$$E(V) = E_0 + \frac{9V_0K_0}{16}\left\{\left[\left(\frac{V_0}{V}\right)^{\frac{2}{3}} - 1\right]^3 K_0' + \left[\left(\frac{V_0}{V}\right)^{\frac{2}{3}} - 1\right]^2 \left[6 - 4\left(\frac{V_0}{V}\right)^{\frac{2}{3}}\right]\right\}, \tag{7}$$

where V_0 is the equilibrium volume, E and E_0 are the cohesive energy and the cohesive energy of equilibrium volume, respectively, K_0 and K_0' are the bulk modulus and its first derivative over pressure, respectively. Its comparison with experimental data is shown in Table 1. The lattice

parameters are slightly overestimated in comparison with the experimental ones, except for V. The maximum error is, however, less than 1%. The predicted bulk moduli show also excellent agreement with experimental values measured at 4.2 K with a mean error lower than 4%. The vanadium bulk modulus prediction is, however, overestimated by 14%.

Total energies were calculated using the Monkhorst-Pack mesh [37] of k-points in the Brillouin zone, with k-mesh spacing of 0.2 Å^{-1}. This corresponds to 14×14×14 k-point meshes for a two-atom BCC cubic cell. The plane wave cut-off energy used in the calculations was 400 eV. The total energy convergence criterion was set to 10^{-5} eV/cell and force components were relaxed to 10^{-3} eV/Å.

Table 1: Unit cell parameters a_{DFT} and bulk moduli K_{DFT} obtained by DFT simulations for pure elements, compared with the corresponding experimental results a_{exp} and K_{exp}.

	a_{DFT} (pm)	a_{exp} (pm)	K_{DFT} (GPa)	K_{exp} (GPa)
Mo	316.93	314.7[38]	262	260[38], 265[39]
Nb	332.17	330.04[38]	172	172[38], 172[40]
Ta	332.10	330.3[38]	197	190[38], 198[41]
V	299.43	302.4[38]	183	156[38], 160[42]
W	318.98	316.5[38]	304	310[38], 311[41]

2.2 Monte Carlo simulations and model set up

The most stable or energetically favourable atomic configurations are studied by quasi-canonical Monte Carlo simulations where the ECI parameters obtained from CE are applied. This allows the analysis of the order dependence with temperature in the alloy. In a preliminary analysis, simulating cells containing 2000 atoms in the form of 10×10×10 *primitive* BCC unit cells were considered. MC simulations were performed using the ATAT package [30] starting from a disordered high-temperature state at T = 3000 K, followed by cooling with temperature steps of ΔT = 100 K, and 2000 Monte Carlo steps per atom at both thermalisation and accumulation stages. The evolution of the structure of the five-component HEA is shown in Figure 2. The structures obtained at 800 K and 3000 K are disordered, which shows that the optimised structure at 800 K is still a random solid solution with eventually only small short-range ordering. At 300 K, the

optimised structure of this alloy is decomposed into pure elements as V and Nb atoms, represented by green and red colours in Figure 2, and intermetallic phases as Mo-Ta and V-W.

This technique is used for the DFT model set-up for the 300 K and 800 K simulations, while the pre-melting structures are generated by applying special quasi-random structures (SQSs) [43] which enable to model random configurations in a relatively small cell, and represent the configurations of fully disordered solid solutions at the high temperature limit. SQSs were generated using a method based on a Monte Carlo simulated annealing loop [44] as implemented in the ATAT package [30].

The interatomic spacing distribution in a random configuration of atoms is studied by applying SQSs in simulations containing 128 atoms in the form of 4×4×4 primitive unit cells in nearly-equiatomic composition. We will adopt the notation HEA for the equimolar five-component MoNbTaVW and HEA/W, HEA/V, HEA/Ta, HEA/Nb and HEA/Mo for equimolar four-component systems without W, V, Ta, Nb and Mo atoms, respectively. The dependence of the interatomic spacing distribution of such compositions with temperature and consequent chemical order is studied in a set of 54 atom simulations in 3×3×3 primitive unit cells, for the pre-melting (SQSs generated), 800 K and 300 K (MC generated) conditions.

2.3 DFT structure relaxation

The phase stability and structural properties of the generated structures have been investigated by full DFT relaxations with respect to atom (ion) coordinates, volumes and shapes allowed to be changed.

The enthalpies of mixing for structures containing 54 atoms are given in Table 2. For all systems, a systematic increase of mixing enthalpy from low to high temperatures is found. Among all considered multicomponent alloys only HEA/Mo has a small positive enthalpy of mixing with values from 1 meV to 13 meV for the most ordered structure to disordered structures, respectively. The most negative enthalpy of mixing is -105 meV for the HEA/V structure obtained from simulations at 300 K. The energy difference between mixing enthalpies of the HEA, HEA/Mo, HEA/Ta and HEA/W structures generated at 800 K and SQSs is lower than 10 meV, showing that the structures of these alloys at 800 K are similar in terms of energy to the fully random solid solutions.

The values of lattice parameters of five- and four-component HEAs structures generated from MC simulations at 300 K and 800 K and SQSs are given in Table 2. In agreement with the trend for pure elements, the HEA/V displays the largest lattice parameter whereas the HEA/Ta and HEA/Nb have the smallest ones. Similar to the trend of enthalpies of mixing for the 300 K, 800 K and SQS structures, it is found a systematic increase in lattice parameter from ordered to disordered structures. From Table 2, it can be seen that both trends are correlated; an increment of 0.01 pm in a is followed, in average, with increment of 5 meV in ΔH_{mix}.

There is a striking relationship between properties of multicomponent alloys and those of their constituents in terms of chemical bonding and physical properties. We found a strong correlation between cohesive energies (related to enthalpies of mixing), lattice parameters and bulk moduli which are associated with the electronic structure of BCC transition metals between groups VB and VIB in the periodic table. This can be understood from the main contribution of d-orbitals to the cohesive properties of BCC transition metals. For elements in Group VIB (W and Mo), the d band is half filled compared with partially filled for those in Group VB (V, Nb and Ta). This causes larger cohesive energies, smaller lattice parameters and consequently larger bulk moduli for elements in Group VIB. Another effect is related to the fact that the $5d$ band width is larger in comparison with those of $3d$ and $4d$ bands. Therefore the corresponding cohesive energies and bulk moduli of the $5d$ elements are larger in comparison with the $3d$ and $4d$ elements within the same group [45].

Table 2: Unit cell parameters a and enthalpies of mixing ΔH_{mix} obtained by DFT simulations with 54 atoms for the HEA MoNbTaVW and its corresponding sub-quaternary systems for structures generated using MC simulations at 300 K, 800 K and SQS.

	DFT at 300 K		DFT at 800 K		DFT at SQS	
54 atom simulations	a (pm)	ΔH_{mix} (meV/atom)	a (pm)	ΔH_{mix} (meV/atom)	a (pm)	ΔH_{mix} (meV/atom)
HEA	319.85	-61	319.83	-47	319.89	-37
HEA/V	324.34	-105	324.41	-94	324.44	-70
HEA/Nb	317.24	-90	317.35	-74	317.37	-59
HEA/Ta	316.72	-56	316.74	-41	316.81	-37
HEA/Mo	321.26	1	321.46	7	321.43	13
HEA/W	320.51	-47	320.68	-16	320.73	-9

3 Interatomic bond lengths in multicomponent alloys

Figure 3a shows the energy dependence as a function of lattice parameter from DFT calculations for the pure BCC metals Mo, Nb, Ta, V and W. These dependence can be used to model the potential energy of interatomic Mo–Mo, Nb–Nb, Ta–Ta, V–V and W–W interactions. This potential energies will be denoted as U_{ii} and they have been calculated in steps of 1 pm round each corresponding unit cell parameter a_{ii}. Locally, the behaviour of the potentials around the equilibrium position is approximately quadratic. This stems from the elastic properties of the corresponding elements. A parabola has been fitted to each calculated potential. The unit cell parameter of each element a_{ii} is displayed with a square, and the mean second neighbour distance for each i–i interaction, obtained from the i–i interactions of the 128 atom simulation with composition MoNbTaVW at SQS condition, denoted r_{ii}, is shown in circles. There is a clear tendency to displace the i–i interactions from a_{ii} towards the unit cell parameter of the alloy. For instance, the V–V second neighbour mean distance in the lattice is $r_{VV} = 313$ pm, while the unit cell parameter of V is $a_{VV} = 299$ pm. Equivalently, the V–V nearest neighbour mean distance shows a larger value in the simulations than the nearest neighbour distance in the V lattice. That means that the V–V interactions are in tension with respect to the equilibrium distances of the pure V rigid lattice. Thus, the V–V interaction applies a force towards the V equilibrium distance r_{VV}. On the other hand, being the V–V interaction at equilibrium around r_{VV}, an opposite force of the same magnitude applies, whose origin is the surrounding atoms of the distorted lattice. Equilibrium occurs when the V-V tension equals the lattice force applied on it. Its counterpart cases are Nb–Nb and Ta–Ta interactions, which are in compression with respect to their equilibrium interatomic distances. In other words, the atoms modify the crystal structure, producing a distorted lattice, as well as the lattice affects the atomic bonding behaviour.

In order to analyse the effect of the lattice on the atomic bondings, we will consider a fictitious potential representing the mean behaviour of the lattice U_{lat}. This fictitious potential applies a force opposite to i–i interactions which leads to the equilibrium distances r_{ii} obtained from DFT simulation. The i–i interactions are described by the *ab initio* interatomic potentials U_{ii}, from

which the applied force is derived:

$$F_{ii} = -\frac{dU_{ii}}{dr} \quad ; \quad F_{lat} = -\frac{dU_{lat}}{dr} \tag{8}$$

Then, for any i–i equilibrium distance obtained r_{ii}, the following condition must be satisfied

$$\left.\frac{dU_{ii}}{dr}\right|_{r=r_{ii}} + \left.\frac{dU_{lat}}{dr}\right|_{r=r_{ii}} = 0 \quad ; \quad i = \text{Mo, Nb, Ta, V, W} \tag{9}$$

For the i–j interactions, the cross–potential U_{ij} can be estimated from the elemental U_{ii} potentials with the following mixing rule [46]:

$$U_{ij} = -\big(U_{ii}U_{jj}\big)^{1/2} \tag{10}$$

where the minus sign keeps the negative value of the potential energy around equilibrium. And the force applied between i–j bonds can also be estimated by applying Eq.(8) to U_{ij}.

By using these potentials, the force applied $\left.\frac{dU_{ij}}{dr}\right|_{r=r_{ij}}$ at the obtained mean equilibrium distance r_{ij} due to the i–j interaction nature is calculated, and depicted in Figure 3b. The fictitious potential U_{lat} should satisfy Eq.(9) for all r_{ij} distances. This can be estimated by fitting a straight line to the calculated $\left.\frac{dU_{ij}}{dr}\right|_{r=r_{ij}}$ values. Such values are shown in Figure 3b together with $\frac{dU_{lat}}{dr}$ depicted with a grey line.

U_{lat} potential can be approximated by using the different mixing rules of the elemental potentials U_{ii}. Two mixing rules have been considered for this purpose: firstly, the extension of Eq.(10) to many atomic type interactions U_{prod}; and secondly, a linear combination of the potentials U_{lin}:

$$U_{prod} = -\left(\prod_{k=1}^{n} \left|U_{kk}\right|^{1/n}\right) \quad ; \quad U_{lin} = \big(\sum_{k=1}^{n} U_{kk}\big)\frac{1}{n} \tag{11}$$

The derived $\frac{dU_{prod}}{dr}$ and $\frac{dU_{lin}}{dr}$ can be observed in Figure 3b. Both have reasonable agreement with the fitted $\frac{dU_{lat}}{dr}$ and can be used to estimate the effect of the lattice on the elemental interactions.

The comparison of lattice parameters and bulk moduli computed for structures with 128 atoms

by using the proposed potentials and those obtained from DFT is shown in Table 3. The agreement of unit cell parameters for all considered compositions is good. A mean error between DFT and potentials is slightly larger for U_{lin} than for U_{prod} but in both cases it is lower than 1 pm. The bulk moduli computed using both potentials are slightly overestimated compared with the DFT results where the mean errors for U_{lin} and U_{prod} are 5.35 GPa and 11.75 GPa respectively. Both potentials U_{lin} and U_{prod} show in general good agreement with DFT calculations. U_{lin} provides extraordinary simplicity, being a summation of quadratic polynomials and guarantees its quadratic behaviour around the equilibrium position.

Due to this quadratic behaviour, we can consider now the following expression for the force:

$$F_{ij} = -\frac{dU_{ij}}{dr} = -(2p_1 r + p_2) \quad , \tag{12}$$

where p_1 and p_2 are constants. The following steps aim at identifying p_1 and p_2. In a cubic lattice at equilibrium, the cohesive energy E is determined by the interatomic potential U, and is related to the bulk modulus K and the atomic volume V [47] as:

$$K = \left(V \frac{\partial^2 E}{\partial V^2} \right) = \frac{n_a}{9r} \frac{\partial^2 U}{\partial r^2} \tag{13}$$

where n_a is the number of atoms in the unit cell of length r. In a cubic system at equilibrium $r = a$, this can be expressed as

$$K = \frac{n_a}{9a} \left. \frac{d^2 U}{dr^2} \right|_{r=a} = \frac{n_a}{9a} 2p_1 \tag{14}$$

Thus

$$p_1 = \frac{9}{2n_a} Ka \quad ; \quad p_2 = -\frac{9}{n_a} Ka^2 \tag{15}$$

where p_2 has been calculated by imposing $\left. \frac{dU_{ij}}{dr} \right|_{r=a} = 0$ in Eq.(12). This allows a simple description of the potential and its derived force around equilibrium positions:

$$U_{ii} = \frac{9}{n_a} K_{ii} a_{ii} r(r - 2a_{ii}) + U_{0,ii} \quad ; \quad F_{ii} = -\frac{dU_{ii}}{dr} = \frac{18}{n_a} K_{ii} a_{ii} (a_{ii} - r) \tag{16}$$

where $U_{0,ii}$ is a constant related to the binding energy of each atom. For the calculation of the

forces applied, this term is not relevant.

The unit cell parameters and bulk moduli extracted from the *ab initio* potentials have been compared with the calculated expression for the force at Eq.(16) with $n_a = 2$ in the BCC lattice. The results are shown in Figure 3c, where the dots represent the finite difference for calculating $-\frac{dU_{ii}}{dr}$ from the *ab initio* potential, and the corresponding lines come from Eq.(16). The excellent agreement adds confidence in using Eq.(16) for estimating the interatomic forces.

Table 3: Unit cell parameter a and bulk modulus K obtained by DFT simulations with 128 atoms and estimated values by potentials U_{prod}, U_{lin} and Eq.(23) for the HEA MoNbTaVW and its corresponding sub-quaternary systems.

	Unit cell parameter (pm)				Bulk modulus (GPa)			
128 atom	DFT	Calculated			DFT	Calculated		
simulations	at SQS	U_{prod}	U_{lin}	Eq.(23)	at SQS	U_{prod}	U_{lin}	Eq.(23)
HEA	320.27	319.28	321.01	320.07	216	230.26	223.92	223.25
HEA/V	324.54	323.54	324.17	323.79	228	247.52	241.75	233.39
HEA/Nb	317.03	317.07	318.60	317.82	230	235.16	231.41	236.25
HEA/Ta	317.13	316.78	318.41	317.40	224	233.07	228.68	229.76
HEA/Mo	321.42	320.11	322.25	321.07	204	219.80	214.31	213.44
HEA/W	320.87	319.38	321.76	320.52	196	214.30	203.87	202.93
Mean error		0.8633	0.9467	0.4633	Mean error	13.68	7.66	6.84

4 Methodology for lattice description in multicomponent alloys

A methodology for computing the mean interatomic distances and atomic coordinates for a given combination of atomic positions is presented here. The previously derived expressions for interatomic potentials will be employed. The data extracted from *ab initio* simulations will be used to compare the obtained interatomic distances and atomic coordinates by this methodology.

4.1 Unit cell parameter and bulk modulus

The calculation of both lattice parameter and bulk modulus in the alloy is of paramount importance since they define the potential U_{lat}. By using the linear mixing rule in Eq.(11), the computation of

U_{lin} is simple and approximates both the cross–interatomic potentials U_{ij} and the lattice potential U_{lat} for a certain composition. Lets examine first an equimolar binary system. The following expressions for the potentials are considered:

$$\begin{cases} U_{ii} &= \frac{9}{n_a} K_{ii} a_{ii} r(r - 2a_{ii}) + U_{0,ii} \\ U_{jj} &= \frac{9}{n_a} K_{jj} a_{jj} r(r - 2a_{jj}) + U_{0,jj} \\ U_{ij} &= \frac{9}{n_a} K_{ij} a_{ij} r(r - 2a_{ij}) + U_{0,ij} \approx \frac{1}{2}\Big(U_{ii} + U_{jj}\Big) \end{cases} \tag{17}$$

For the polynomial operation properties:

$$K_{ij} a_{ij} \approx \frac{1}{2}\Big(K_{ii} a_{ii} + K_{jj} a_{jj}\Big) \quad ; \quad K_{ij} a_{ij}^2 \approx \frac{1}{2}\Big(K_{ii} a_{ii}^2 + K_{jj} a_{jj}^2\Big) \tag{18}$$

which can be easily resolved:

$$a_{ij} \approx \frac{a_{ii}^2 K_{ii} + a_{jj}^2 K_{jj}}{a_{ii} K_{ii} + a_{jj} K_{jj}} \quad ; \quad K_{ij} \approx \frac{1}{2} \frac{\big(a_{ii} K_{ii} + a_{jj} K_{jj}\big)^2}{a_{ii}^2 K_{ii} + a_{jj}^2 K_{jj}} \tag{19}$$

For any composition X_i, X_j of elements i and j, the potential for the binary system reads

$$U_{ij} \approx X_i U_{ii} + X_j U_{jj} \tag{20}$$

whose general solution is

$$a_{ij} \approx \frac{a_{ii}^2 K_{ii} X_i + a_{jj}^2 K_{jj} X_j}{a_{ii} K_{ii} X_i + a_{jj} K_{jj} X_j} \quad ; \quad K_{ij} \approx \frac{\big(a_{ii} K_{ii} X_i + a_{jj} K_{jj} X_j\big)^2}{a_{ii}^2 K_{ii} X_i + a_{jj}^2 K_{jj} X_j} \tag{21}$$

Which can be extended to a multicomponent alloy in solid solution

$$U_{lat} \approx \sum_{i=1}^{n} X_i U_{ii} \tag{22}$$

and

$$a_{lat} \approx \frac{\sum_{i=1}^{n} a_{ii}^2 K_{ii} X_i}{\sum_{i=1}^{n} a_{ii} K_{ii} X_i} \quad ; \quad K_{lat} \approx \frac{\big(\sum_{i=1}^{n} a_{ii} K_{ii} X_i\big)^2}{\sum_{i=1}^{n} a_{ii}^2 K_{ii} X_i} \tag{23}$$

It follows that, the unit cell parameter and bulk modulus are intimately related and cannot be treated separately. It is worth noting that both a_{lat} and K_{lat} behave nearly linearly if, across all elements, both the elemental unit cell parameters and bulk moduli are close to each other.

The calculation of a_{lat} and K_{lat} from Eq.(23) has been compared with the results obtained from DFT calculations and shown in Table 3. The agreement is excellent and improves the results given by U_{prod} and U_{lin}, showing a mean error lower than 0.5 pm and a maximum error of 0.79 pm for the case HEA/Nb. The mean bulk modus error is 4.34 GPa with a maximum of 5.44 GPa for HEA/Nb.

4.2 Interatomic distance matrix S

The interatomic distance matrix S defined in Eq.(2) describes the lattice distortion and can be used for modelling SSH and other properties of the alloys. The elements of the matrix S are at the equilibrium distances of each first neighbours atomic type interaction. This can be calculated by resolving Eq.(9), which uses second neighbour distance as variable, leading to the equilibrium second neighbour distance r_{ij}, and expressing this solution in terms of the first neighbour distance $r_{ij} = s_{ij}/f$, which for each i–j interaction reads:

$$\left.\frac{dU_{ij}}{dr}\right|_{r=\frac{s_{ij}}{f}} + \left.\frac{dU_{lat}}{dr}\right|_{r=\frac{s_{ij}}{f}} = 0 \quad ; \quad i,j = \text{Mo, Nb, Ta, V, W} \tag{24}$$

By using Eq.(16) for calculating the force $\dfrac{dU_{ij}}{dr}$, the description of a_{ij} and K_{ij} at Eq.(21) and a_{lat} and K_{lat} in Eq.(23), the system Eq.(24) can be expressed as

$$K_{ij}a_{ij}(a_{ij} - r) + K_{lat}a_{lat}(a_{lat} - r) = 0 \quad , \quad i,j = \text{Mo, Nb, Ta, V, W} \tag{25}$$

Note that, from Eq.(21) and Eq.(23)

$$K_{ij}a_{ij} = \frac{1}{2}\left(a_{ii}K_{ii} + a_{jj}K_{jj}\right) \quad , \quad K_{lat}a_{lat} = \sum_{i=1}^{n} a_{ii}K_{ii}X_i \tag{26}$$

And then, the elements of matrix S are approximated by

$$s_{ij} = f\frac{K_{ij}a_{ij}^2 + K_{lat}a_{lat}^2}{K_{ij}a_{ij} + K_{lat}a_{lat}} \quad , \quad i,j = \text{Mo, Nb, Ta, V, W} \tag{27}$$

This solution represents the mean equilibrium distance for each i–j interaction resulting from a random distribution of atoms, which is represented by U_{lat}. This scenario is better captured by the simulation with more atoms and SQS distribution, since it guarantees arbitrary neighbours. The application of Eq.(27) for computing the matrix S of interatomic distances has been compared with the mean interatomic spacing distances obtained for each i–j interaction type in the HEA MoNbTaVW and the corresponding sub-quaternary systems simulated. This has been done by considering the distribution $\langle\xi\rangle$ of distances:

$$\langle\xi\rangle = \left\{||\boldsymbol{\chi_p} - \boldsymbol{\chi_q}||\right\}_{p=1,\ldots,m\ ;\ q=N_{(p)1}} \tag{28}$$

computed from the atomic coordinates $\boldsymbol{\chi_p} = (\chi_p^1,\ \chi_p^2,\ \chi_p^3)$ obtained from DFT simulation, for all atoms in the simulation, where $N_{(p)1}$ denotes the set of first neighbours for atom p. From the distribution $\langle\xi\rangle$, the mean value of all pairs of atoms with the same i–j elements is computed, leading to the interatomic spacing matrix S_{DFT}:

$$S_{DFT} = \left\{\bar{\xi}_{ij}\right\}_{i,j=\text{Mo, Nb, Ta, V, W}} \tag{29}$$

where $\bar{\xi}_{ij}$ denotes the mean value of all first neighbour distances found between i and j atoms. The results can be observed in Figure 4 for 128 atom simulations showing excellent agreement with Eq.(27). A mean quadratic error E_{mean} lower than 1.1 pm across all simulations is observed as indicated in Figure 4, together with the maximum value E_{max} of the quadratic error. The error bars account for a 95% standard error in the computation of the mean from the set of interatomic spacing distances obtained by DFT simulation. The variation of S with composition is well described by the model.

The trend for the interatomic spacing distances in MoNbTaW alloy is consistent with results obtained by using *ab initio* molecular dynamics [32]. However, the values obtained in this work

are generally larger than in [32], where the local density approximation [48] was applied. This approximation tends to over-bind materials in comparison with GGA-PBE used in this work.

The case of chemical order is displayed by simulations at lower temperatures. This is plotted in Figure 5 for simulations with 54 atoms at SQS, 800 K and 300 K together with their mean and maximum errors. Eq (27) calculations display larger errors for the lower temperatures simulated, underlying the decrease of randomness in atomic positions.

We can conclude that, for a certain composition, S is not constant as long as chemical order occurs, but the difference with respect to the mean value which represents a random configuration of atoms keeps within values well below 2 pm. The particular configuration of atoms in each simulation is then responsible for this difference. In the next section the development of a method to calculate this contribution by computing the atomic coordinates of a certain configuration is presented. Their mean values will be just a consequence of this computation.

4.3 Interatomic spacing distribution

Every interatomic spacing is linked to the rest of the crystal structure spacings it belongs and cannot be calculated in isolation. The main forces acting on an atom in a BCC structure are due to its first and second neighbours, as found by the ECI parameter calculation above. First neighbours are in repulsive interaction, while second neighbours are in attractive interaction. In a cubic lattice without defects, any neighbour j_1 of a certain atom i has its counterpart j_2 at the same distance and in opposite directions. Atomic vibrations impede that the three aligned atoms j_1–i–j_2 belongs to a straight line, but for low temperatures and small lattice distortions, the angle $\widehat{j_1 i j_2}$ is very close to 180 degrees. Thus, the forces F_{ij_1} and F_{ij_2} on i due to j_1–i and i–j_2 interactions respectively will be both repulsive or both attractive, and are balanced since they act in opposite directions. Since the atom i is at equilibrium, positive displacements will follow negative forces and vice-versa. For small displacements, quadratic behaviour of the interatomic potentials is expected, and a linear approximation of the combined force $F_{ij_1} + F_{ij_2}$ is possible, by considering a coupled spring system between j_1–i and i–j_2, whose equilibrium results from mean equilibrium distances as described in Eq.(27). The addition of all first and second neighbours of atom i creates a spring system in a three-dimensional cubic array, where the first 8 neighbours of

an atom i are linked to it by springs with equilibrium at distance s_{ij}, and its second 6 neighbours are linked to atom i by springs at an equilibrium distance a_{ij}, where j is the corresponding atom type for each case.

The force exerted per interaction is computed by deriving the potentials U_{ij} in Eq.(17) for the three spatial coordinates x^l $(l = 1, 2, 3)$, as described by Eq.(16)

$$\frac{dU_{ij}}{dx_l} = \frac{18}{n_a} K_{ij} a_{ij} x^l \Big(1 - \frac{a_{ij}}{||\boldsymbol{x}||}\Big) \quad , \tag{30}$$

where $||\boldsymbol{x}||$ is the norm of the vector $\boldsymbol{x} = (x^1, x^2, x^3)$. By applying Eq.(30) to all atoms in the simulation, equilibrium is reached when the summation of all forces applied becomes 0 in the three spatial directions. This is mathematically expressed as:

$$\begin{aligned} 0 \;=\; W\frac{18}{n_a} \sum_{q=N_{(p)1}} K_{ij} s_{ij} (x_p^l - x_q^l)\Big(1 - \frac{s_{ij}}{||\boldsymbol{x_p} - \boldsymbol{x_q}||}\Big) + \\ \frac{18}{n_a} \sum_{q=N_{(p)2}} K_{ij} a_{ij} (x_p^l - x_q^l)\Big(1 - \frac{a_{ij}}{||\boldsymbol{x_p} - \boldsymbol{x_q}||}\Big) \end{aligned} \Bigg|_{\substack{l=1,2,3 \\ p=1,\ldots,m}} \tag{31}$$

where $N_{(p)1}$ and $N_{(p)2}$ are the indices of the first and second neighbours respectively of atom p, m the number of atoms in the simulation, and the subscripts i and j at K_{ij}, s_{ij} and a_{ij} correspond to the respective i and j atomic type for atoms numbered as p and q respectively. W accounts for the weighted contribution of the first neighbour and second neighbours on i, due to its distance and geometrical configuration. W is expected to be > 1. Its value has been fitted to minimise the error of the computed interatomic distances extracted from the final configuration and the corresponding computed by DFT simulation. Expressed in terms of the packing factor f, its value is $W = (2/f)^2$.

Considering an initial rigid BCC lattice where the atoms are at ideal positions $\boldsymbol{x}_{0,p} = (x^1_{0,p}, x^2_{0,p}, x^3_{0,p})$, where the unit cell parameter is calculated by Eq.(23), and equilibrium occurs for atomic displacements $\boldsymbol{\Delta x}_p = (\Delta x^1_p, \Delta x^2_p, \Delta x^3_p)$ around their initial ideal position. The common factor $\dfrac{18}{n_a}$ in Eq. (31) can be ignored, and denoting $x_{0,pq} = x^l_{0,p} - x^l_{0,q}$ and $\Delta x^l_{pq} = \Delta x^l_p - \Delta x^l_q$, Eq.(31) becomes:

$$
\begin{aligned}
0 \;=\; W \sum_{p=N_{(p)1}} K_{ij} s_{ij} (x^l_{0,pq} + \Delta x^l_{pq}) \Big(1 - \frac{s_{ij}}{||\boldsymbol{x_{0,pq}} + \boldsymbol{\Delta x_{pq}}||}\Big) + \\
\sum_{p=N_{(p)2}} K_{ij} a_{ij} (x^l_{0,pq} + \Delta x^l_{pq}) \Big(1 - \frac{a_{ij}}{||\boldsymbol{x_{0,pq}} + \boldsymbol{\Delta x_{pq}}||}\Big)
\end{aligned}
\Bigg|_{\substack{l=1,2,3 \\ p=1,...,m}} =
$$

$$
= \sum_{j=N_{(p)1},N_{(p)2}} K_{ij} f_W a_{ij} (x^l_{0,pq} + \Delta x^l_{pq}) \Big(1 - \frac{f a_{ij}}{||\boldsymbol{x_{0,pq}} + \boldsymbol{\Delta x_{pq}}||}\Big) \Bigg|_{\substack{l=1,2,3 \\ p=1,...,m}} \tag{32}
$$

where $f_W = W\dfrac{\sqrt{3}}{2} = \dfrac{4}{f}$ for p in the atoms at $N_{(p)1}$ and $f_W = 1$ at $N_{(p)2}$, and $f = \dfrac{\sqrt{3}}{2}$ is the packing factor for BCC as defined in Eq.(3).

This leads to a system of $3m$ equations whose variables are Δx^l_p, for $l = 1, 2, 3$ and atoms $p = 1, ..., m$. No close-form expression has been found for this system and a numerical method has been implemented to solve it. By applying Newton's equations of motion, a second differential order system is derived from Eq.(32), which calculates the force acting on every atom by means of the relative positions of its neighbours and the atomic mass of each atom M_p:

$$
\left\{ \begin{array}{rcl}
\dfrac{d^2 x^l_1}{dt^2} M_1 & = & - \displaystyle\sum_{q=N_{(1)1}N_{(1)2}} K_{ij} f_W a_{ij} (x^l_{1q}) \Big(1 - \frac{f a_{ij}}{||\boldsymbol{x_{1q}}||}\Big) \\
\vdots & & \\
\dfrac{d^2 x^l_m}{dt^2} M_m & = & - \displaystyle\sum_{q=N_{(m)1}N_{(m)2}} K_{ij} f_W a_{ij} (x^l_{mq}) \Big(1 - \frac{f a_{ij}}{||\boldsymbol{x_{mq}}||}\Big)
\end{array} \right| _{l=1,2,3} \tag{33}
$$

with initial conditions:

$$
\left\{ \begin{array}{rcl} x^l_p & = & x^l_{0p} \end{array} \right| _{\substack{l=1,2,3 \\ p=1,...,m}} \tag{34}
$$

For each atom p, the solution of this system is an oscillator, whose trajectory moves around a certain mean position. The set of mean positions corresponds to the solution satisfying Eq.(32), vanishing the summation of forces over each atom. In order to obtain these mean positions, a dumped oscillator is considered on the system defined in Eq.(33), whose friction is proportional to the velocity. The dumped oscillator converges quickly and equilibrium is reached when the atomic displacements Δx^l_p are close to 0 for all atoms and spatial coordinates. The threshold selected for this criteria has been $|\Delta x^l_p| < 10^{-3}$ pm for $p = 1, ..., m$ and $l = 1, 2, 3$. The computational cost of this method for the systems with 128 atoms is in the order of a few seconds in a normal computer.

This method has been applied to a BCC rigid structure with the initial configuration of atoms used in the *ab initio* simulations, as described in Section 2, and the unit cell parameter computed from Eq.(23). In this way, every atom has the same neighbour configuration in both methods. The double spring system solution moves the atomic coordinates towards the same atomic coordinates predicted by DFT simulation. The error of this approximation is displayed by considering the final atomic coordinates $\boldsymbol{x_{i_k}} = \boldsymbol{x_{0,i_k}} + \boldsymbol{\Delta x_{i_k}}$ and computing the distribution of $\langle \varsigma \rangle$ distances

$$\langle \varsigma \rangle = \Big\{ ||\boldsymbol{x_p} - \boldsymbol{x_q}|| \Big\}_{p=1,...,m \ ; \ q=N_{(p)1}} \tag{35}$$

The result can be observed in Figure 6 where each distance in the distribution $\langle \varsigma \rangle$, obtained by solving Eq.(33), is plotted against its corresponding distance in the distribution $\langle \xi \rangle$ from DFT simulations; mean (E_{mean}) and maximum quadratic (E_{max}) errors are also indicated. E_{mean} is lower than 2 pm in all simulations, and $E_{max} = 11.8$ pm for the HEA/W simulation. The results of applying this method to the 54 atom simulations is shown in Figure 7. In these cases, the local differences and dissimilarity with respect to a random configuration are now considered in the model, in contrast with the computation of the mean values with Eq.(27). This is clear, since the errors with respect to the simulations does not increase when short-range order occurs, which happened on applying Eq.(27) for 800 K and 300 K simulations. The mean error is also is lower than 2 pm and the maximum is 8.8 pm.

The simulations are run at 0 K with the equilibrium configuration at 300 K, 800 K and SQS scenarios. The temperature contribution modifies the atomic coordinates around the solution obtained by DFT calculation at 0 K. The range of this variation can be approximated by considering the kinetic energy of an atom $E_k = \frac{3}{2} k_b T$, where k_b is the Boltzmann constant and T the temperature. Such variation can be related to the overall atomic displacement due to the potential energy displayed in Figure 3a for different elements. The obtained possible displacements are in the range of 7–10 pm for 300 K and 10–15pm for 800 K. This demonstrates that the mean accuracy of the predicted coordinates by this methodology is below the contribution of the temperature to the atomic vibrations. Thus, the temperature contribution to atomic displacements due to vibrations will be similar to the error displayed by this method.

Other approaches have provided answer to similar problems, where the equilibrium positions

and atomic displacements of certain systems were considered. Specially remarkable is the Kanzaki's contribution [49] oriented to distortion around defects in cubic lattices. The interatomic spacing distribution in binary systems was studied in Froyen's work [50] were a fictitious mean lattice was considered, from which the atomic coordinates move. In these approaches, an expression of the interatomic potential is needed, which allow the consideration of anharmonic effects due to large distortions and defects. Our approach needs only unit cell parameter and bulk moduli for approximating the nature of the forces involved. It is intended for describing the distortion in a lattice free of defects, were it is assumed that the difference of atomic sizes induces distortions in the elastic regime. This assumption is supported by the obtained results, since the difference with DFT simulations is in the order of 1-2 pm in average value. In addition to that, HEAs satisfy the Hume-Ruthery rules [51, 52], where the atomic size mismatch δ is defined, which accounts for the difference in atomic size of the elements involved. A maximum of $\delta = 6.5\%$ applies for HEAs in solid solution, which highlights the order of magnitude of the distortion and the use of the linear approximations.

In summary, the computed atomic coordinates can be used to accelerate the DFT calculations, avoiding the rigid lattice starting point in favour of a pre-relaxed structure. Figure 8 shows a comparison of the total-energy convergence in DFT relaxations by using the rigid lattice and the pre-relaxed structure as starting points. The total energy of the first step of ionic relaxation is significantly closer to the convergence energy for the pre-relaxed configuration than the initial one. Importantly, both calculations converge to the same value of the total energy demonstrating the validity of the Eq.(23) although the total number of relaxation steps remain the same in this example.

We have used the results of the predicted atomic coordinates by solving Eq.(33), and the corresponding interatomic spacing distribution $\langle\varsigma\rangle$, to calculate the mean values of each i–j interactions, which lead to building the matrix S_{spring} for each composition and temperature.

$$S_{spring} = \left\{\bar{\varsigma}_{ij}\right\}_{i,j=\text{Mo, Nb, Ta, V, W}} \tag{36}$$

where $\bar{\varsigma}_{ij}$ denotes the mean value of all first neighbour distances computed by solving Eq.(33)

between atoms of type i and j.

The results of comparing S_{spring} and S_{DFT} of Eq.(29) computed with the 128 atoms simulations is displayed in in Figure 9, while the corresponding comparison by using the 54 atoms simulation are in Figure 10. Matrix S_{spring} clearly shows an improvement with respect to the predicted S matrix of Eq.(27) for a random configuration of atomic positions. This corresponds to a correction due to the short-range order factor induced by temperature.

5 Conclusions

A methodology to predict the mean interatomic spacing matrix S, its distribution and the atomic coordinates in multicomponent solid solution alloys is presented here. The benchmark alloys are the equimolar HEA MoNbTaVW and its 5 sub-quaternary systems. The description of the forces acting between atoms is described by the use of elemental unit cell parameters and bulk moduli. The interatomic spacing distribution is obtained by imposing force equilibrium for all atomic bonds and the effect of the lattice around them. The results obtained correspond to a random configuration of elemental atomic positions in the BCC lattice and have been compared with *ab initio* DFT simulations, reaching good agreement between both methods. The effect of short-range order, which deviates the lattice configuration from randomness, can be studied by means of a spring system, where the first and second neighbours for each atom are the most influential. A numerical method solves the system of differential equations proposed by the spring system. It has been demonstrated that this method approximates the DFT simulation solution of the atomic coordinates with good agreement. The matrix S can be computed from this solution, which corrects the influence of temperature and short-range order. The method shows mean variations in the range of 1-2 pm with respect to DFT simulations. The atomic coordinates computed by this method can be used as a better starting point for the time consuming DFT simulations and to quantify the solid solution hardening effects in high entropy alloys.

6 Acknowledgements

The authors wish to acknowledge financial support from the Accelerated Metallurgy Project, which is co-funded by the European Commission in the 7th Framework Programme (Contract NMP4-LA-2011-263206), by the European Space Agency and by the individual partner organisations. This work was partially funded by the RCUK Energy Programme through grant no. EP/I501045 and by the United Kingdom Engineering and Physical Sciences Research Council via a programme grant EP/G050031. To obtain further information on the data and models underlying this paper, please contact PublicationsManager@ccfe.ac.uk.

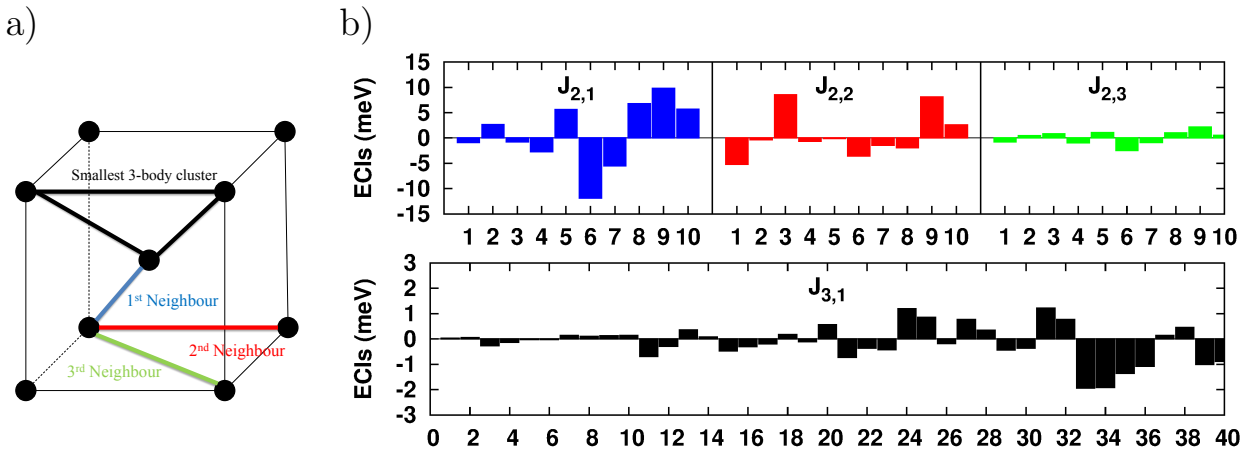

Figure 1: a) Schematic view of the pair clusters in the 1st, 2nd and 3rd nearest neighbour coordination shell and the smallest 3-body cluster, b) Effective cluster interaction parameters $J_{2,1}$, $J_{2,2}$, $J_{2,3}$ and $J_{3,1}$ for pair clusters 1st, 2nd and 3rd nearest neighbour coordination shell 3-body cluster $J_{3,1}$ respectively. The horizontal axis x stands for different clusters decorations by point functions.

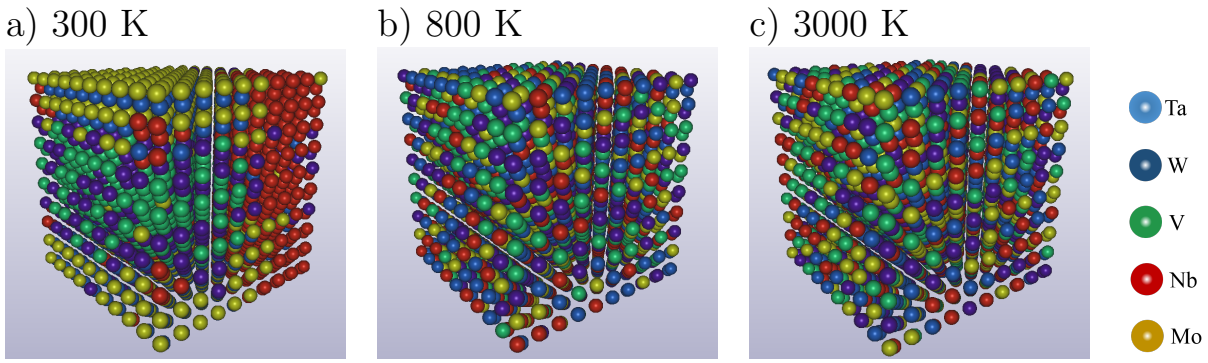

Figure 2: Structures generated using MC simulations at 300 K (a), 800 K (b) and 3000 K (c).

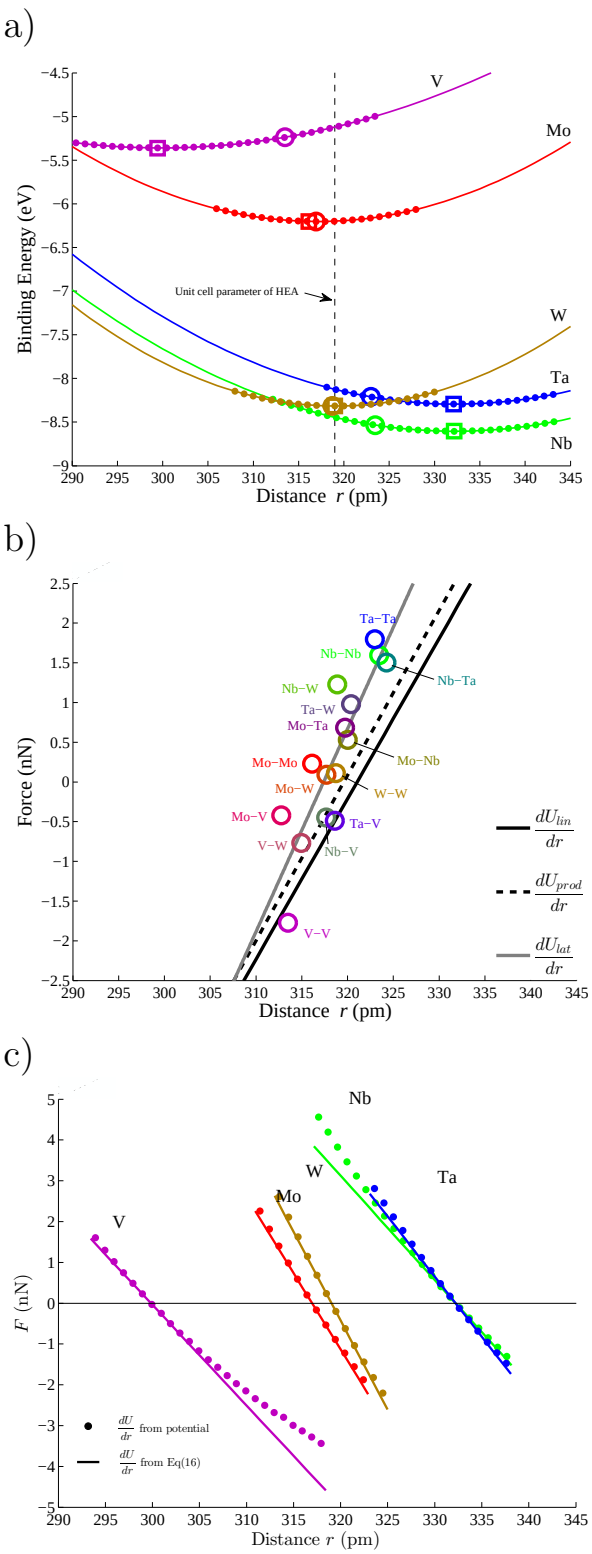

Figure 3: a) Interatomic potentials for Mo, Nb, Ta, V and W, b) Function $\frac{dU_{fic}}{dr}$ and the points with coordinates $\{r_{ij}, -\frac{dU_{ij}}{dr}\big|_{r=r_{ij}}\}$ with i, j = Mo, Nb, Ta, V and W, c) Comparison between the derived $F_{ii} = -\frac{dU_{ij}}{dr}$ and Eq.(16) for Mo, Nb, Ta, V and W interatomic potentials.

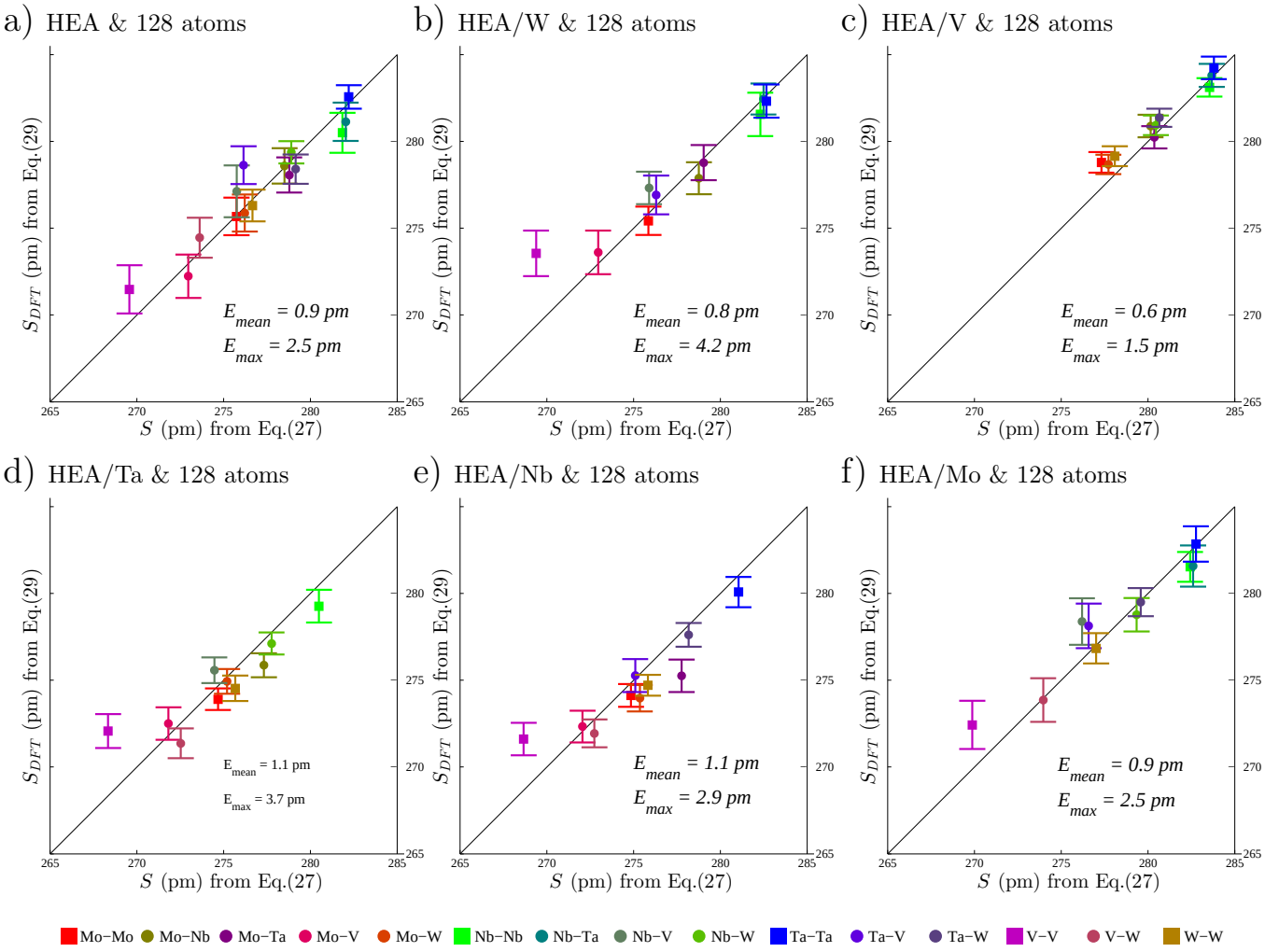

Figure 4: Calculated S matrix by Eq.(27) *vs.* S_{DFT} obtained by 128 atoms simulation by Eq.(29), for the compositions a) HEA, b) HEA/W, c) HEA/V, d) HEA/Ta, e) HEA/Nb and f) HEA/Mo at SQS condition.

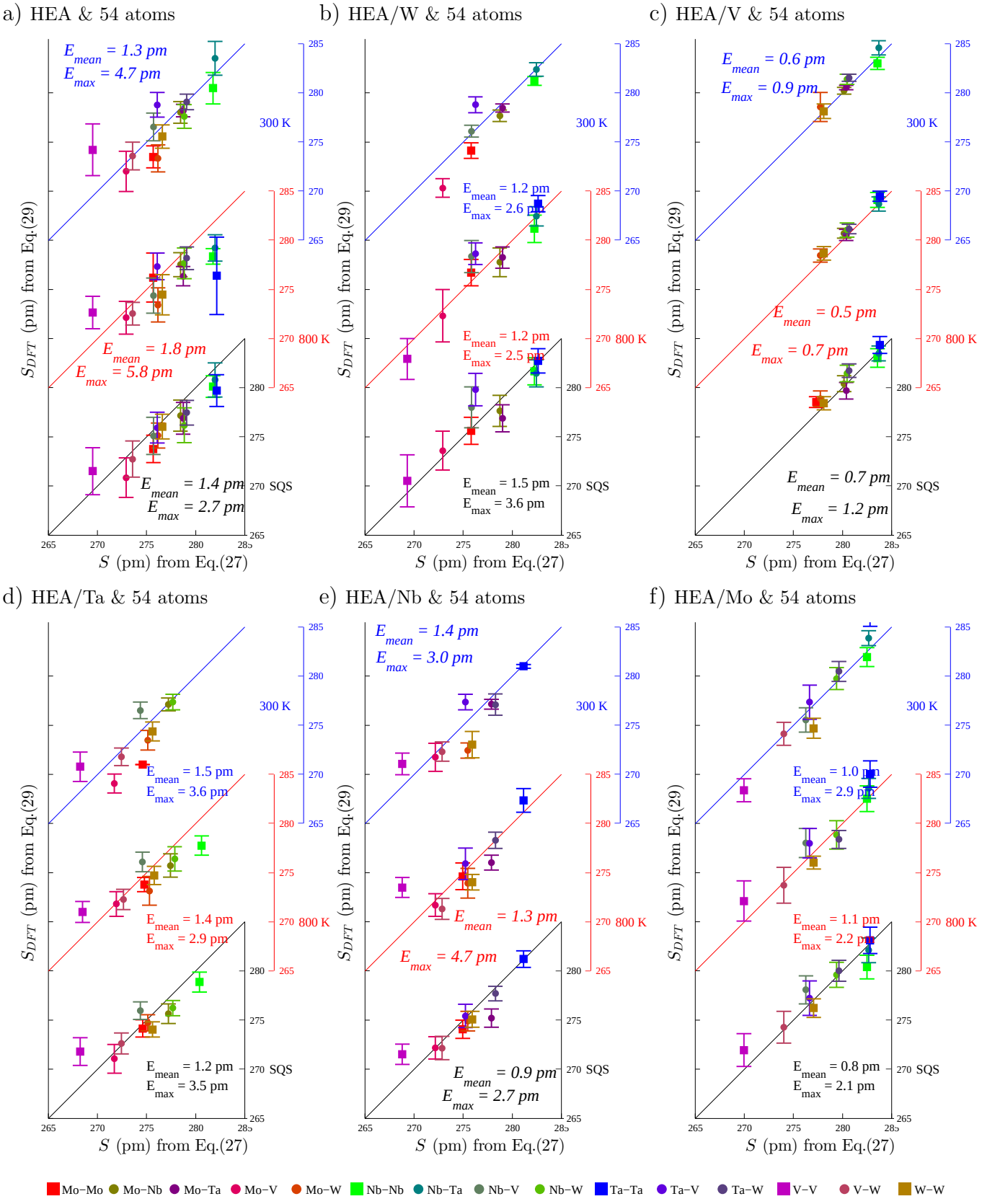

Figure 5: Calculated S matrix by Eq.(27) *vs.* S_{DFT} obtained by 54 atoms simulation by Eq.(29), for the compositions a) HEA, b) HEA/W, c) HEA/V, d) HEA/Ta, e) HEA/Nb and f) HEA/Mo at conditions SQS, 800 K and 300 K.

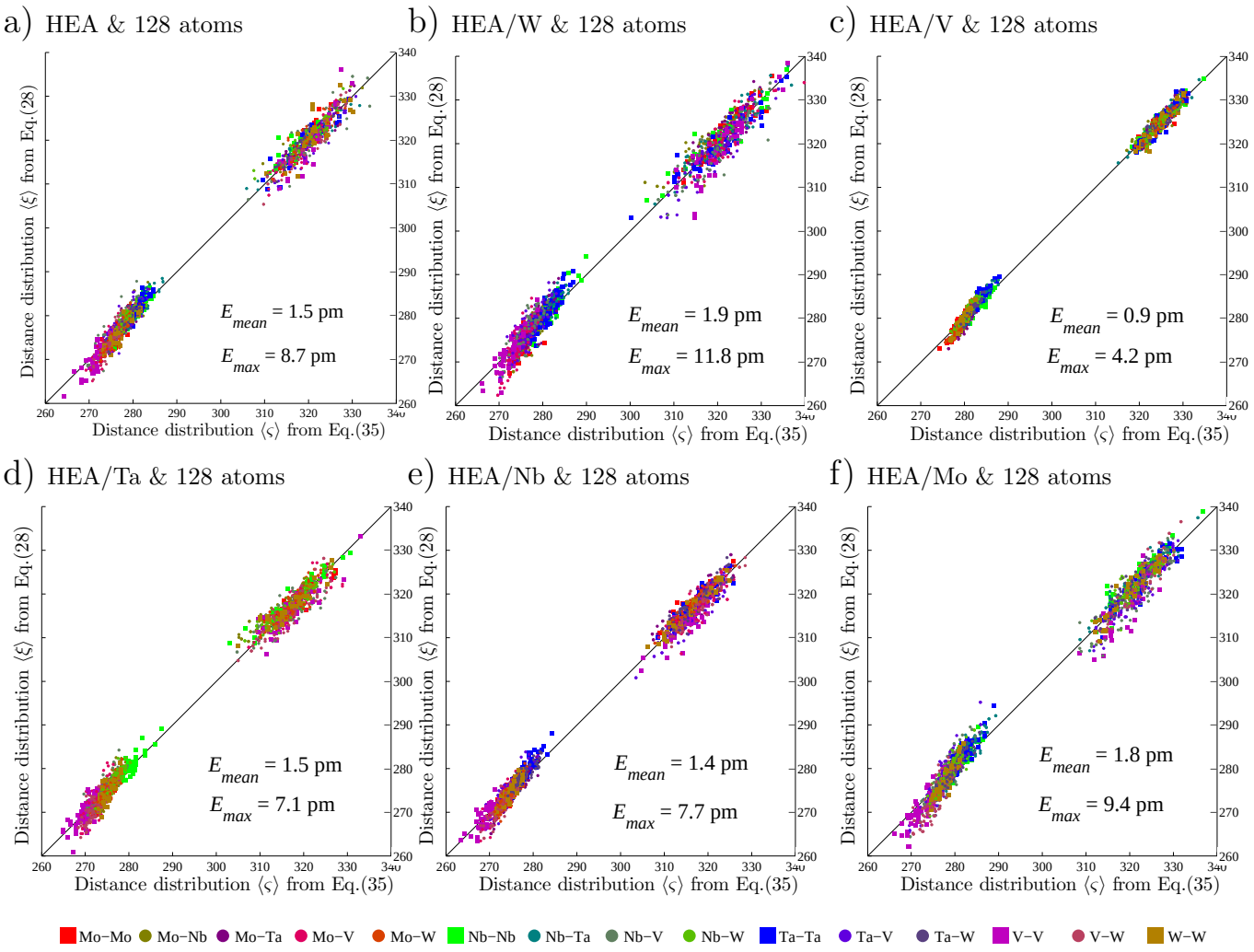

Figure 6: Calculated distance distribution $\langle\varsigma\rangle$ in Eq.(35) by solving Eq.(33) with initial conditions in Eq.(34) *vs.* distance distribution $\langle\xi\rangle$ at Eq.(28) obtained by 128 atoms DFT simulation for the compositions a) HEA, b) HEA/W, c) HEA/V, d) HEA/Ta, e) HEA/Nb and f) HEA/Mo at SQS condition.

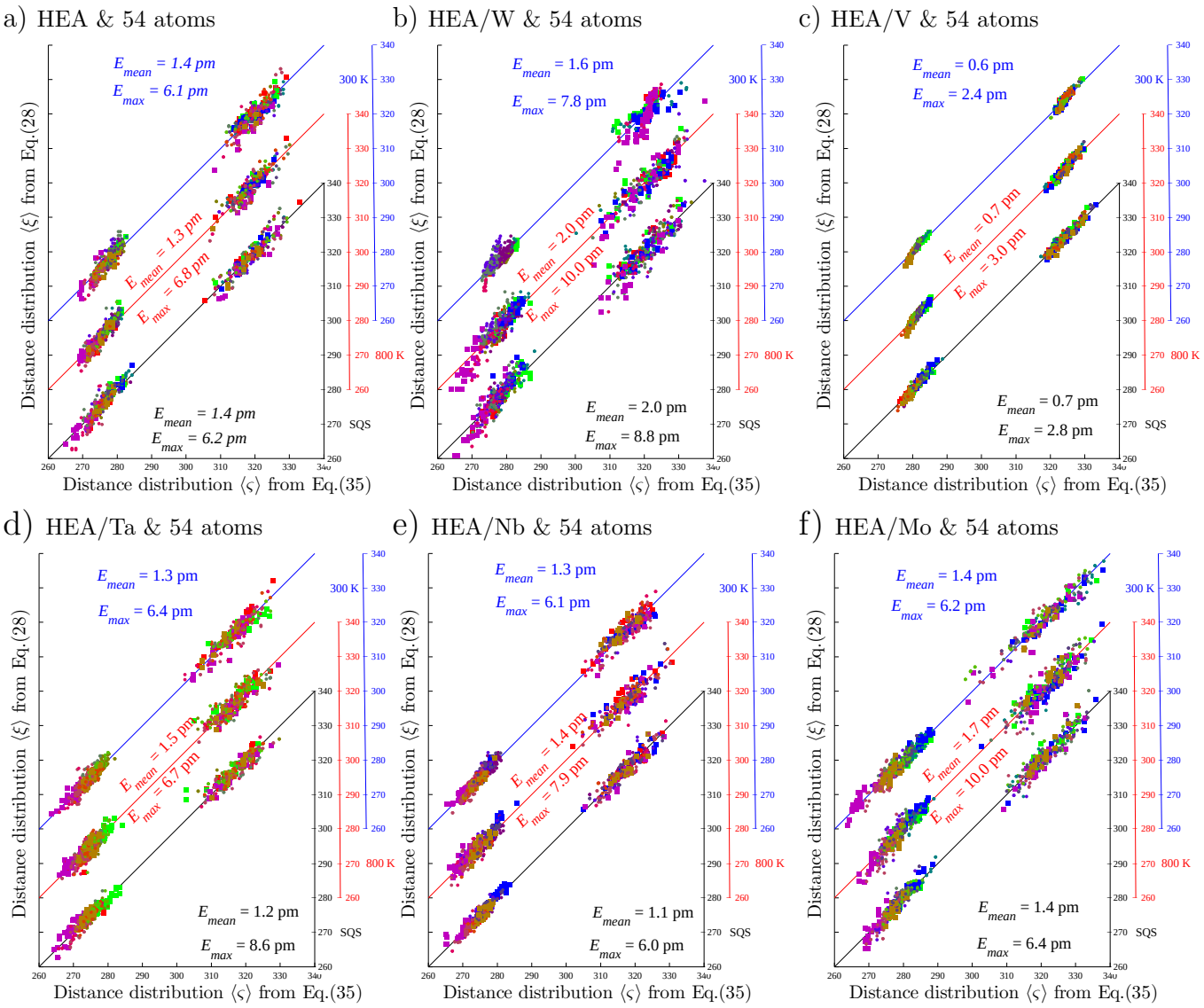

Figure 7: Calculated distance distribution $\langle\varsigma\rangle$ in Eq.(35) by solving Eq.(33) with initial conditions in Eq.(34) *vs.* distance distribution $\langle\xi\rangle$ at Eq.(28) obtained by 54 atoms DFT simulation for the compositions a) MoNbTaVW, b) MoNbTaV, c) MoNbTaW, d) MoNbVW, e) MoTaVW and f) NbTaVW at conditions SQS, 800 K and 300 K.

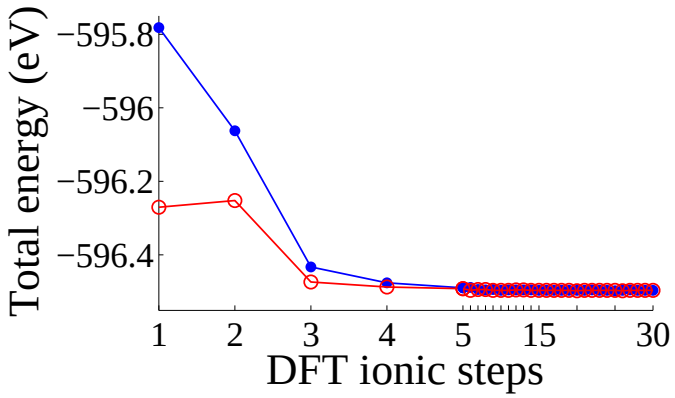

Figure 8: Total-energy convergence study by DFT relaxations between the two cases in the HEAs: conventional procedure from non-relaxed structures in blue solid dots and the use of pre-relaxed structures generated by Eq. (23) in red circle symbols.

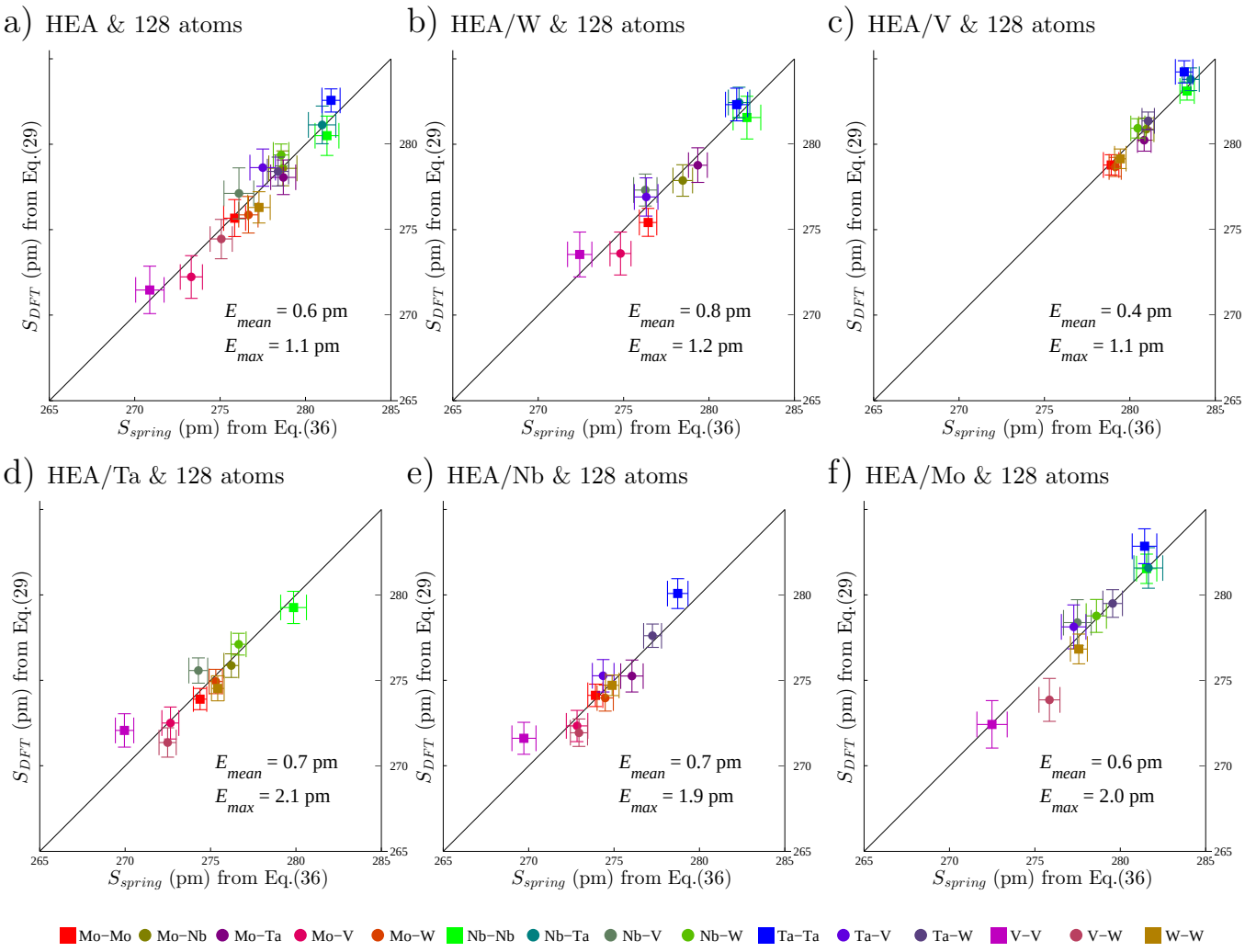

Figure 9: Calculated S_{spring} matrix at Eq.(36) after solving Eq.(33) with initial conditions at Eq.(34) *vs.* S_{DFT} obtained by 128 atoms simulation by Eq.(29), for the compositions a) HEA, b) HEA/W, c) HEA/V, d) HEA/Ta, e) HEA/Nb and f) HEA/Mo at condition SQS.

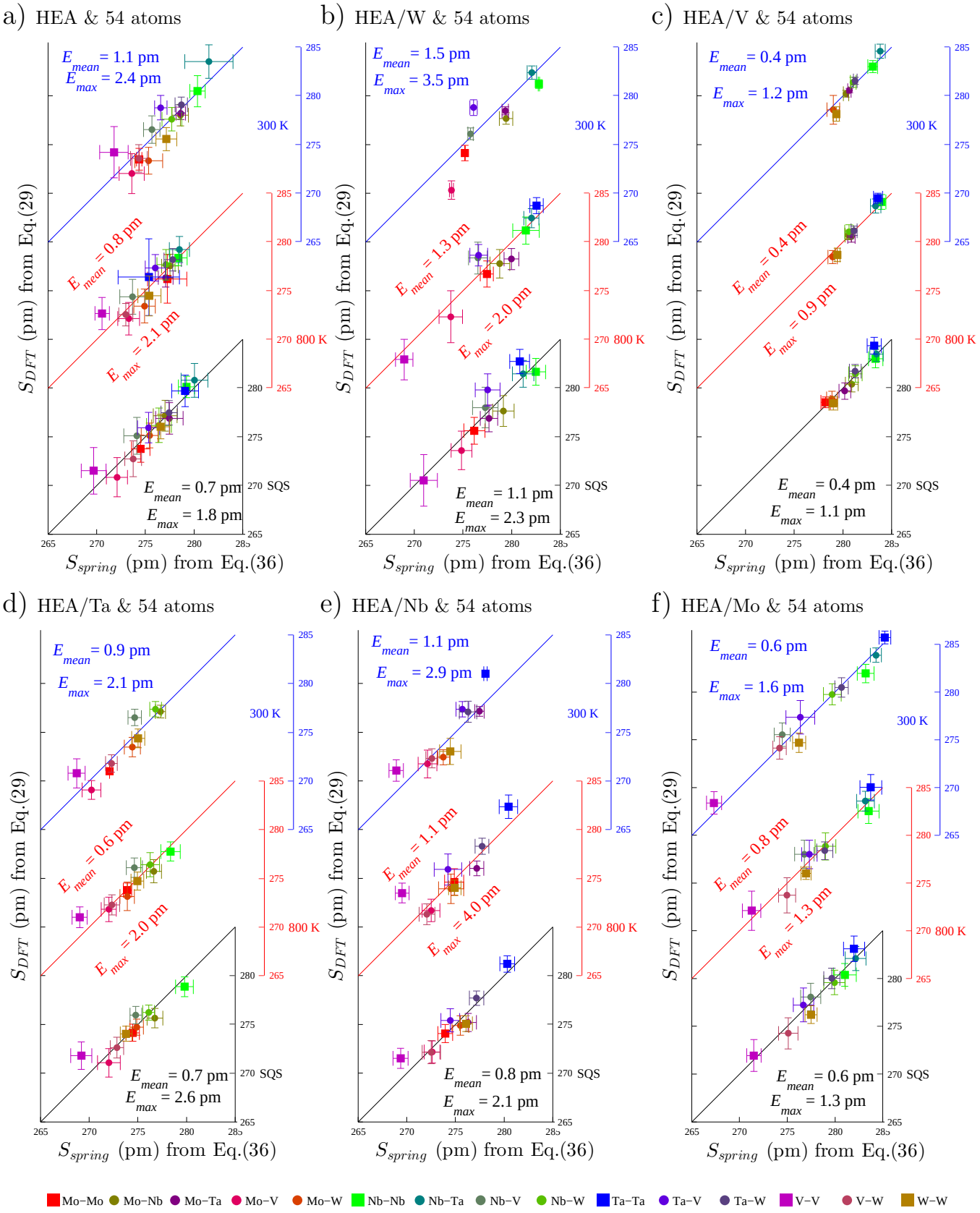

Figure 10: Calculated S_{spring} matrix at Eq.(36) after solving Eq.(33) with initial conditions at Eq.(34) *vs.* S_{DFT} obtained by 54 atoms simulation by Eq.(29), for the compositions a) HEA, b) HEA/W, c) HEA/V, d) HEA/Ta, e) HEA/Nb and f) HEA/Mo at conditions SQS, 800 K and 300 K.

References

[1] J. W. Yeh, S. K. Chen, S. J. Lin, J. Y. Gan, T. S. Chin, T. T. Shun, C. H. Tsau, and S. Y. Chang. *Advanced Engineering Materials*, 6:299–203, 2004.

[2] Y. Zhang, Y. J. Zhou, J. P. Lin, G. L. Chen, and P. K. Liaw. *Advanced Engineering Materials*, 10:534–538, 2008.

[3] C. Y. Hsu, J. W. Yeh, S. K. Chen, and T. T. Shun. *Metallurgical and Materials Transactions A*, 35A:1465–1469, 2004.

[4] O. N. Senkov, G. B. Wilks, J.M. Scott, and D.B. Miracle. *Intermetallics*, 11:698–706, 2011.

[5] O. N. Senkov, S. V. Senkova, B. Miracle, and C. Woodward. *Materials Science & Engineering A*, 565:51–61, 2013.

[6] F. Otto, C. Somsen A. Dlouhý and, H. Bei, G. Eggeler, and E.P. George. *Acta Materialia*, 61:5743–5755, 2013.

[7] E. P. George A. Gali. *Intermetallics*, 39:74–78, 2013.

[8] A. V. Kuznetsov, D. G. Shaysultanov, N. D. Stepanov, G.A. Salishchev, and O.N. Senkov. *Materials Science and Engineering A*, 533:107–118, 2012.

[9] O. N. Senkov, S. V. Senkova, and C. Woodward. *Acta Materialia*, 68:214–228, 2014.

[10] F. J. Wang, Y. Zhang, and G. L. Chen. *Journal of Alloys and Compounds*, 478:321–324, 2009.

[11] Y. Zhang, T. T. Zuo, Z. Tang, M. C. Gao, K. A. Dahmen, P. K. Liaw, and Z. P. Lu. *Progress in Materials Science*, 61:1–93, 2014.

[12] W. R. Wang, W. L. Wang, and J. W. Yeh. *Journal of Alloys and Compounds*, 589:143–152, 2014.

[13] C. J. Tong, M. R. Chen, S. K. Chen, J. W. Yeh, T. T. Shun, S. J. Lin, and S. Y. Chang. *Metallurgical and Materials Transactions A*, 36A:1263–1271, 2005.

[14] R. Sriharitha, B. S. Murty, and R. S. Kottada. *Journal of Alloys and Compounds*, 583:419–426, 2014.

[15] R. Labusch, J. Ahearn G. Grange, and P. Haasen. *Rate processes in plastic deformation of materials*. American Society for Metals, Cleveland, 1975.

[16] I. Toda-Caraballo and P. E. J. Rivera-Díaz del Castillo. *Acta Materialia*, 85:14–23, 2014.

[17] R. L. Fleischer. *Acta Metallurgica*, 11:203–209, 1963.

[18] L. Čižek. *Journal of Materials Science Metallurgica*, 9:1517–1520, 1974.

[19] L. A. Gypen and A. Deruyttere. *Journal of Material Science*, 12:1028–1033, 1977.

[20] H. A. Moreen, R. Tagaart, and D. H. Polonis. *Metallurgical Transactions*, 2:265–268, 1971.

[21] K. D. Liss, A. B. Bartels, A. Schreyer, and H. Clemen. *Textures and Microstructures*, 35:219–252, 2003.

[22] F. Körmann, A. A. H. Breidi, S. L. Dudarev, N. Dupin, G. Ghosh, T. Hickel, P. Korzhavyi, J. A. Muñoz, , and I. Ohnuma. *Physica status solidi*, 251:53–80, 2014.

[23] J. S. Wróbel, D. Nguyen-Manh, M. Y. Lavrentiev, M. Muzyk, and S. L. Dudarev. *Physical Review B*, 91:024108, 2015.

[24] M. C. Gao and D. E. Alman. *Entropy*, pages 4504–4519, 2013.

[25] J. M. Sanchez, F. Ducastelle, and D. Gratias. *Pyhsica A*, 128:334–350, 1984.

[26] O. N. Senkov, G. B. Wilks, D. B. Miracle, C. P. Chuang, and P. K. Liaw. *Intermetallics*, 18:1758–1765, 2010.

[27] B. Cantor, I. T. H. Chang, P. Knight, and J. B. Vincent. *Materials Science and Engineering: A*, 375-377:213–218, 2004.

[28] S. Singh, N. Wanderka, B. S. Murty, U. Glatzel, and J. Banhart. *Acta Materialia*, 59:182–190, 2011.

[29] A. van de Wall. *Calphad*, 33:266–278, 2009.

[30] A. van de Walle, M. Asta, and G. Ceder. *Calphad*, 26(4):539–553, 2002.

[31] W. P. Huhn and M. Widom. *JOM*, 65:1772–1779, 2013.

[32] M. Widom, W. P. Huhn, S. Maiti, and W. Steurer. *Metallurgical & Materials Transactions A*, 45:196–200, 2013.

[33] G. Kresse and J. Furthmüller. *Computational Materials Sciciencd*, 6:15–50, 1996.

[34] G. Kresse and J. Furthmüller. *Physical Review B*, 54:11169–11186, 1996.

[35] J. P. Perdew, K. Burke, and M. Ernzerhof. *Physical Review Letters*, 77:3865–3868, 1996.

[36] F. Birch. *Physical Review*, 71:809, 1947.

[37] H. J. Monkhorst and J. D. Pack. *Physical Review B*, 13:5188–5192, 1976.

[38] D. R. Lide ed. *CRC Handbook of Chemistry and Physics*. CRC Press, Boca Raton, FL., 2005.

[39] F H Featherston. *The elasticconstants of tantalum, tungsten and molybdenum*. United States Naval Postgraduate School, Monterey, California, 1963.

[40] D. J. Hayes and F. R. Brotzen. *Journal Applied Physics*, 45(4):1721, 1974.

[41] C. E. Anderson and F. R. Brotzen. *Journal of Applied Physics*, 53:292–297, 1982.

[42] D. I. Bolef, R. E. Smith, and J. G. Mille. *Physical Review B*, 3:4100, 1971.

[43] A. Zunger, S. H. Wei, L. G. Ferreira, and J. E. Bernard. *Physical Review Lettters*, 65(3):353–356, 1990.

[44] A. van de Walle, P. Tiwary, M. de Jong, D. L. Olmsted, M. Asta, A. Dick, D. Shin, Y. Wang, L. Q. Chen, and Z. K. Liu. *Calphad*, 42:13–18, 2013.

[45] D. Pettifor. *Bonding and structures of molecules and solids*. Clarendon Press, Oxford, 1995.

[46] H. Rafii-Tabar and A. P. Sutton. *Philosophical Magazine Letters*, 63:217–224, 1991.

[47] R. Gaudoin, W. M. C. Foulkes, and G. Rajagopal. *Journal of Physics Condensed Matter*, 14:87878–8793, 2002.

[48] W. Kohn and L. J. Sham. *Physical Review*, 140:A1133–A1138, 1965.

[49] H. Kanzaki. *Journal of Physics and Chemistry of Solids*, 2:24–36, 1957.

[50] S. Froyen and C. Herring. *Journal of Applied Physics*, 52:7165–7173, 1981.

[51] A. Takeuchi and A. Inoue. *Materials Transactions JIM*, 41:1372–1378, 2000.

[52] A. Takeuchi and A. Inoue. *Materials Science and Engineering A*, 304–306:446–451, 2001.